Journal of Computational Physics 231 (2012) 5910–5925

Contents lists available at SciVerse ScienceDirect

Journal of Computational Physics

journal homepage: www.elsevier.com/locate/jcp

A parallel fast algorithm for computing the Helmholtz integral operator in 3-D layered media

Min Hyung Cho [a], Wei Cai [a,b,*]

[a] Department of Mathematics and Statistics, University of North Carolina at Charlotte, Charlotte, NC 28223-0001, USA
[b] Institute of Natural Sciences, Shanghai Jiaotong University, Shanghai 200240, PR China

ARTICLE INFO

Article history:
Received 17 September 2011
Received in revised form 12 April 2012
Accepted 13 May 2012
Available online 26 May 2012

Keywords:
Helmholtz equation
Layered media
Green's function
Window function
Fast multipole method
Tree-code

ABSTRACT

In this paper, we propose a parallel fast algorithm for computing the product of the discretized Helmholtz integral operator in layered media and a vector in $O(N_q N_z^2 N_x N_y \log N_x N_y)$ operations. Here $N_x N_y N_z$ is the number of sources and N_q is the number of quadrature points used in the evaluation of the Sommerfeld integral in the definition of layered media Green's function (for problems in thin-layer media, $N_z = O(1)$). Such a product forms the key step of many iterative solvers (such as the Krylov subspace based GMRES and BiCG-STAB) for linear systems arising from the integral equation methods for the Helmholtz equations. The fast solver is based on two important techniques which reduce the cost of quadrature summations in the Sommerfeld contour integral for Green's functions in 3-D layered media. The first technique is the removal of surface pole effects along the real axis integration contour by identifying the pole locations with a discrete wavelet transform; In the second technique, we apply a window-based high frequency filter to shorten the contour length. As a result, the integral operator for the 3-D layered media can be efficiently written as a sum of 2-D Hankel cylindrical integral operators, and the latter can be calculated by either a tree-code or a 2-D wideband fast multipole method in a fast manner. Numerical results show the efficiency and parallelism of the proposed fast algorithm.

1. Introduction

The electromagnetic simulation of scattering from objects embedded in a homogeneous or layered structure has many practical applications ranging from geoscience to quantum mechanics. Among the many numerical techniques, integral equation methods [19,25] have several advantages over the conventional finite difference method [32] or finite element method [30], such as the built-in radiation conditions at infinity, easy mesh generations for complex geometries, and a reduced number of unknowns. However, the main issue with integral equation methods in layered media, in contrast to the case of homogeneous media where fast solvers such as the fast multipole method (FMM) are available, is the lack of a fast solver for the dense matrix system arising from the discretized integral equation.

In general, to solve the matrix equation from the integral equation, a Krylov subspace based iteration method, such as GMRES [29] or BiCGSTAB [31], is used. A main step for the iterative solver involves the product of the matrix and a vector. A direct multiplication will cost $O(N^2)$ operations for a full $N \times N$ matrix. Many algorithms exist for a homogeneous background medium to reduce this cost to the order of $O(N)$ or $O(N \log N)$; among them are the FMM [27,28], the adaptive integral method (AIM) [3], and the FFT method [4]. However, the speed-up of integral equation methods for layered media still faces

* Corresponding author at: Department of Mathematics and Statistics, University of North Carolina at Charlotte, Charlotte, NC 28223-0001, USA.
E-mail address: wcai@uncc.edu (W. Cai).

0021-9991/$ - see front matter © 2012 Elsevier Inc. All rights reserved.
http://dx.doi.org/10.1016/j.jcp.2012.05.022

much challenges. There have been several attempts to construct fast integral methods for layered media [20]. The natural way is to formulate the scattering problems using Green's functions of the layered media. As the layered media Green's function is expressed as a Hankel transform, defined in terms of the Sommerfeld integral, its calculation is time consuming and also dictates how the Helmholtz integral operator can be implemented. Many methods have been proposed to address the difficulties of the Sommerfeld integral, for example, the complex image method (CIM) via Prony's approximation [2,12], the fast Hankel transform [22], and the steepest decent path for the Sommerfeld integration [13,14,24]. In this paper, techniques such as high frequency filtering and an adaptive quadrature formula (with surface pole identification by a discrete wavelet transform) will be used to minimize the cost of computing the Helmholtz integral operator. The key component of the fast algorithm relies on decomposing the integral operator for the 3-D layered media as a series of operators defined by cylindrical waves (Hankel kernels) within a range of wave numbers resulting from the quadrature formula for the Sommerfeld integral. The cylindrical wave integral operator will be then implemented by a local expansion tree-code for the Bessel function and a wideband FMM (wFMM) [9–11,15], and the latter can be downloaded from http://fastmultipole.org/ [16].

This paper will be organized as follows: in Section 2, the spectral form of the Green's function will be derived and validated with known analytical solutions. Section 3 starts with the Green's function in physical space using the Hankel transform, and then techniques mentioned above are presented to minimize the quadrature cost in the contour integral for the Hankel transform. In Section 4, we will present the fast algorithm for implementing the Helmholtz integral operator in 3-D layered media with the local expansion tree-code and wFMM, and numerical performance of the proposed fast algorithms for thin-layer structures will also be presented. Conclusions are given in Section 5.

2. Spectral form for Green's functions in layered media

The 3-D scalar Helmholtz equation with a point source at $\mathbf{r}' = (0, 0, z')$ in an N-layer structure (Fig. 1) with layer locations $d_i,\ 0 \leqslant i \leqslant N-1$, is defined by the following equation,

$$\nabla \frac{1}{m_i} \nabla G_i(\mathbf{r}, \mathbf{r}') + k_i^2 G_i(\mathbf{r}, \mathbf{r}') = -\delta(\mathbf{r}, \mathbf{r}'), \quad i = 0, 1, \ldots, N, \tag{1}$$

where i indicates the ith layer. By taking the Fourier transform in the horizontal plane to transform x and y to spectral variables k_x and k_y, respectively, we obtain

$$\frac{d}{dz}\frac{1}{m_i}\frac{d}{dz}\widehat{G}_i(k_x, k_y, z; z') - (k_\rho^2 - k_i^2)\widehat{G}_i(k_x, k_y, z; z') = -\frac{1}{2\pi}\delta(z - z'), \tag{2}$$

where

$$k_\rho^2 = k_x^2 + k_y^2. \tag{3}$$

Due to cylindrical symmetry in the (k_x, k_y) variables, Eq. (2) simplifies to

$$\frac{d}{dz}\frac{1}{m_i}\frac{d}{dz}\widehat{G}_i(k_\rho, z; z') - u_i^2\widehat{G}_i(k_\rho, z; z') = -\frac{1}{2\pi}\delta(z - z'), \tag{4}$$

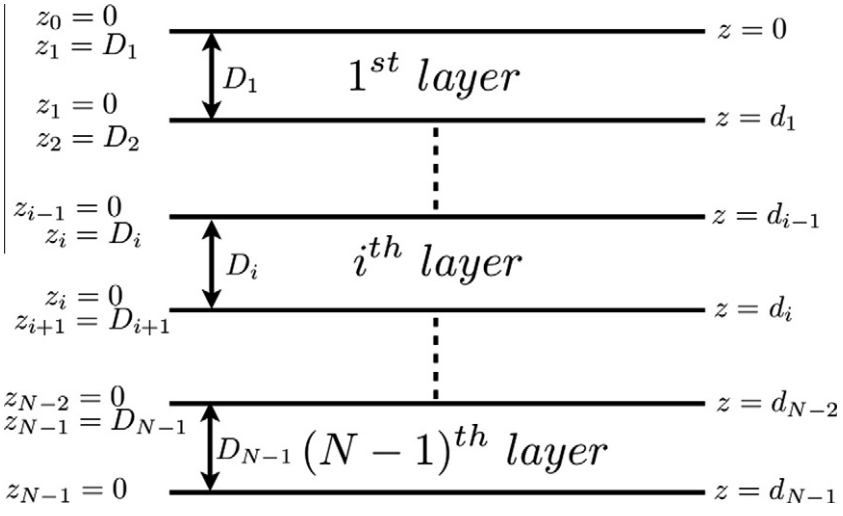

Fig. 1. Layered structure with a local coordinate system, $z_i = z - d_i$.

where

$$u_i^2 = k_\rho^2 - k_i^2. \tag{5}$$

Now the system of ordinary differential equation (4) can be solved analytically for each interval in z while imposing the matching conditions between the ith and $(i-1)$th layer,

$$\alpha_{i-1}\widehat{G}_{i-1} = \alpha_i \widehat{G}_i, \tag{6}$$

$$\beta_{i-1}\frac{d}{dz}\widehat{G}_{i-1} = \beta_i \frac{d}{dz}\hat{G}_i, \tag{7}$$

where

$$\alpha_i = 1 \quad \text{and} \quad \beta_i = \frac{1}{m_i}. \tag{8}$$

Additionally, some decay conditions in the top- and bottom-most layers will be needed for $z \to \pm\infty$.

2.1. Layer without a source

We first consider the ith layer without a source, where the right hand side of Eq. (4) become zero, the solution can be written as a linear combination of cosh and sinh with unknown coefficients a_i and b_i, namely,

$$\widehat{G}_i = a_i \cosh(\sqrt{m_i}u_i z_i) + b_i \sinh(\sqrt{m_i}u_i z_i), \tag{9}$$

where the local coordinate z_i is defined by

$$z_i = z - d_i. \tag{10}$$

Applying the interface condition Eqs. (6) and (7) at $z_i = D_i$ or $z_{i-1} = 0$ (here D_i denotes the width of the ith layer), we obtain the relationship between the unknown coefficients in the ith and $(i-1)$th layer as

$$a_{i-1}\cosh(\sqrt{m_{i-1}}u_{i-1}0) + b_{i-1}\sinh(\sqrt{m_{i-1}}u_{i-1}0) = a_i\cosh(\sqrt{m_i}u_i D_i) + b_i\sinh(\sqrt{m_i}u_i D_i), \tag{11}$$

$$\frac{1}{m_{i-1}}u_{i-1}a_{i-1}\sinh(\sqrt{m_{i-1}}u_{i-1}0) + \frac{1}{m_{i-1}}u_{i-1}b_{i-1}\cosh(\sqrt{m_{i-1}}u_{i-1}0) = \frac{1}{m_i}u_i a_i \sinh(\sqrt{m_i}u_i D_i) + \frac{1}{m_i}u_i b_i \cosh(\sqrt{m_i}u_i D_i), \tag{12}$$

namely,

$$a_{i-1} = a_i\cosh(\sqrt{m_i}u_i D_i) + b_i\sinh(\sqrt{m_i}u_i D_i), \tag{13}$$

$$b_{i-1} = a_i\frac{m_{i-1}u_i}{m_i u_{i-1}}\sinh(\sqrt{m_i}u_i D_i) + b_i\frac{m_{i-1}u_i}{m_i u_{i-1}}\cosh(\sqrt{m_i}u_i D_i). \tag{14}$$

As a result, the coefficient $(a_{i-1}, b_{i-1})^T$ is related to $(a_i, b_i)^T$ through a transfer matrix $T_{i-1,i}$ as follows:

$$\begin{pmatrix} a_{i-1} \\ b_{i-1} \end{pmatrix} = T_{i-1,i}\begin{pmatrix} a_i \\ b_i \end{pmatrix}, \tag{15}$$

where

$$T_{i-1,i} = \begin{pmatrix} \cosh(\sqrt{m_i}u_i D_i) & \sinh(\sqrt{m_i}u_i D_i) \\ \frac{m_{i-1}u_i}{m_i u_{i-1}}\sinh(\sqrt{m_i}u_i D_i) & \frac{m_{i-1}u_i}{m_i u_{i-1}}\cosh(\sqrt{m_i}u_i D_i) \end{pmatrix}. \tag{16}$$

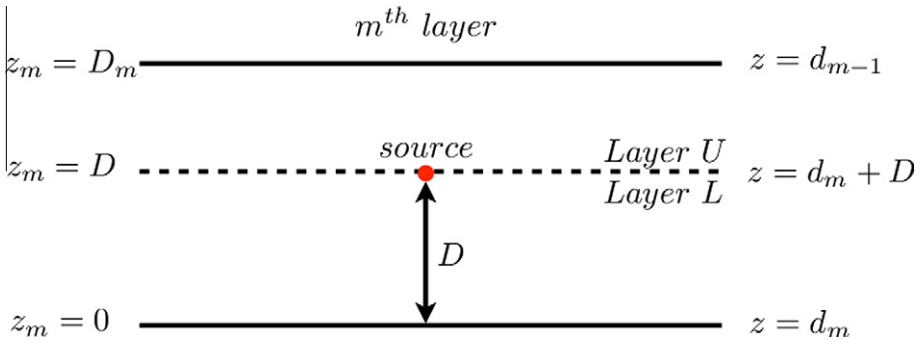

Fig. 2. The mth layer with a source.

2.2. Layer with a source

In the case that a source is located at $z_m = D$ in the mth layer, we divide the mth layer into an upper (U) and lower (L) layer based on the source location as in Fig. 2. In the upper and lower layer, the solutions can be written as

$$\widehat{G}_m^U = a_m^U \cosh(\sqrt{m_m}u_m(z_m - D)) + b_m^U \sinh(\sqrt{m_m}u_m(z_m - D)), \quad D < z_m < D_m, \tag{17}$$

$$\widehat{G}_m^L = a_m^L \cosh(\sqrt{m_m}u_m z_m) + b_m^L \sinh(\sqrt{m_m}u_m z_m), \quad 0 < z_m < D, \tag{18}$$

respectively. At the interface $z_m = D$, we have the following conditions,

$$\alpha_m \widehat{G}_m^U - \alpha_m \widehat{G}_m^L = 0, \tag{19}$$

$$\beta_m \frac{d}{dz}\widehat{G}_m^U - \beta_m \frac{d}{dz}\widehat{G}_m^L = -\frac{1}{2\pi}, \tag{20}$$

where $\alpha_m = 1$ and $\beta_m = \frac{1}{m_m}$. The second condition Eq. (20) can be inferred from the differential equation (4), which requires that the first derivative of $\beta_m \hat{G}$ has a step jump of $-1/2\pi$ to produce the Dirac delta function on the right hand side of Eq. (4). These interface conditions imply

$$a_m^U \cosh(\sqrt{m_m}u_m 0) + b_m^U \sinh(\sqrt{m_m}u_m 0) = a_m^L \cosh(\sqrt{m_m}u_m D) + b_m^L \sinh(\sqrt{m_m}u_m D), \tag{21}$$

$$u_m a_m^U \sinh(\sqrt{m_m}u_m 0) + u_m b_m^U \cosh(\sqrt{m_m}u_m 0) = u_m a_m^L \sinh(\sqrt{m_m}u_m D) + u_m b_m^L \cosh(\sqrt{m_m}u_m D) - \frac{m_m}{2\pi}, \tag{22}$$

resulting in the equations

$$a_m^U = a_m^L \cosh(\sqrt{m_m}u_m D) + b_m^L \sinh(\sqrt{m_m}u_m D), \tag{23}$$

$$b_m^U = a_m^L \sinh(\sqrt{m_m}u_m D) + b_m^L \cosh(\sqrt{m_m}u_m D) - \frac{m_m}{2\pi u_m}. \tag{24}$$

Therefore, one can have the coefficients in the upper layer expressed in matrix form in terms of the coefficients in the lower layer by

$$\begin{pmatrix} a_m^U \\ b_m^U \end{pmatrix} = C_m \begin{pmatrix} a_m^L \\ b_m^L \end{pmatrix} + S_m, \tag{25}$$

where

$$C_m = \begin{pmatrix} \cosh(\sqrt{m_m}u_m D) & \sinh(\sqrt{m_m}u_m D) \\ \sinh(\sqrt{m_m}u_m D) & \cosh(\sqrt{m_m}u_m D) \end{pmatrix} \tag{26}$$

and

$$S_m = \begin{pmatrix} 0 \\ -\frac{m_m}{2\pi u_m} \end{pmatrix} \equiv \begin{pmatrix} 0 \\ c \end{pmatrix}. \tag{27}$$

2.3. Multilayers with a source

In general, the coefficient in the jth layer $V_j = (a_j, b_j)^T$ can be found recursively using Eqs. (15) and (25) as follows:

$$V_j = T_{j,j+1}T_{j+1,j+2}T_{j+2,j+3}\cdots T_{N-1,N}V_N = \prod_{k=j+1}^{N} T_{k-1,k}V_N, \quad j > m, \tag{28}$$

$$V_j = T_{j,j+1}T_{j+1,j+2}\cdots T_{m-1,m}\{C_m(T_{m,m+1}T_{m+1,m+2}\ldots T_{N-1,N}V_N) + S_m\} = \prod_{k=j+1}^{m} T_{k-1,k}\left\{C_m \prod_{k=m+1}^{N} T_{k-1,k}V_N + S_m\right\}, \quad j < m. \tag{29}$$

The top- and bottom-layer coefficients (V_0 and V_N) can be obtained using the solutions $\widehat{G}_0$ and $\widehat{G}_N$ at both ends of the structure, namely,

$$\hat{G}_0 = a_0 \cosh(\sqrt{m_0}u_0 z) + b_0 \sinh(\sqrt{m_0}u_0 z) = \frac{a_0 + b_0}{2}\exp(\sqrt{m_0}u_0 z) + \frac{a_0 - b_0}{2}\exp(-\sqrt{m_0}u_0 z), \tag{30}$$

$$\hat{G}_N = a_N \cosh(\sqrt{m_N}u_N z) + b_N \sinh(\sqrt{m_N}u_N z) = \frac{a_N + b_N}{2}\exp(\sqrt{m_N}u_N z) + \frac{a_N - b_N}{2}\exp(-\sqrt{m_N}u_N z). \tag{31}$$

In order to have proper decay of the solution at both ends of the layered structure, the first term in Eq. (30) and the second term in Eq. (31) should be zero. Thus,

$$a_0 = -b_0, \tag{32}$$
$$a_N = b_N. \tag{33}$$

Finally, the system of algebraic equations between V_0 and V_N can be found from Eq. (29) as

$$\begin{pmatrix} a_0 \\ -a_0 \end{pmatrix} = \prod_{k=1}^{m} T_{k-1,k} C_m \prod_{k=m+1}^{N} T_{k-1,k} V_N + \prod_{k=1}^{m} T_{k-1,k} S_m = \begin{pmatrix} x_{11} & x_{12} \\ x_{21} & x_{22} \end{pmatrix} \begin{pmatrix} a_N \\ a_N \end{pmatrix} + \begin{pmatrix} y_{11} & y_{12} \\ y_{21} & y_{22} \end{pmatrix} \begin{pmatrix} 0 \\ c \end{pmatrix}, \tag{34}$$

which can be solved for a_0 and a_N as follows:

$$a_N = \frac{-c(y_{12} + y_{22})}{x_{11} + x_{12} + x_{21} + x_{22}}, \tag{35}$$
$$a_0 = \frac{-c(x_{11} + y_{12})(y_{12} + y_{22})}{x_{11} + x_{12} + x_{21} + x_{22}} + c y_{12}. \tag{36}$$

Additionally, the initial and terminal conditions for the half-space with perfect electric conductor ($z < 0$) are derived to provide verification of the formula. In the terminal layer, the solution can be written as

$$\hat{G}_N = a_N \cosh(\sqrt{m_N} u_N z_N) + b_N \sinh(\sqrt{m_N} u_N z_N), \tag{37}$$

where $0 \leqslant z_N \leqslant D_N$, and it must be zero at the lower boundary ($z_N = 0$). Therefore,

$$a_N \cosh(\sqrt{m_N} u_N 0) + b_N \sinh(\sqrt{m_N} u_N 0) = a_N = 0 \tag{38}$$

and the conditions for a_0 and b_0 are the same as before. Again from Eq. (29), the system of algebraic equations for a_0 and b_N is found to be

$$\begin{pmatrix} a_0 \\ -a_0 \end{pmatrix} = \prod_{k=1}^{m} T_{k-1,k} C_m \prod_{k=m+1}^{N} T_{k-1,k} V_N + \prod_{k=1}^{m} T_{k-1,k} S_m \equiv \begin{pmatrix} x_{11} & x_{12} \\ x_{21} & x_{22} \end{pmatrix} \begin{pmatrix} 0 \\ b_N \end{pmatrix} + \begin{pmatrix} y_{11} & y_{12} \\ y_{21} & y_{22} \end{pmatrix} \begin{pmatrix} 0 \\ c \end{pmatrix} \tag{39}$$

and it is solved for a_0 and b_N in the half-space as

$$a_0 = \frac{-c x_{12}(y_{12} + y_{22})}{x_{12} + x_{22}} + c y_{12}, \tag{40}$$
$$b_N = \frac{-c(y_{12} + y_{22})}{x_{12} + x_{22}}. \tag{41}$$

Finally, once the correct unknown coefficient V_j is found from Eq. (28) and the terminal condition V_N, the spectral domain Green's function $\hat{G}_j(k_\rho, z; z')$ can be written as

$$\hat{G}_j = V_j \cdot (\cosh(\sqrt{m_j} u_j (z - d_j)), \sinh(\sqrt{m_j} u_j (z - d_j))), \tag{42}$$

if $j \neq m$ or $j = m$ and $z < z'$ and

$$\hat{G}_j = V_j \cdot (\cosh(\sqrt{m_j} u_j (z - z')), \sinh(\sqrt{m_j} u_j (z - z'))), \tag{43}$$

if $j = m$ and $z > z'$.

2.4. Validation of the spectral Green's function

In order to validate the spectral form of Green's function for a layered structure, we conduct a consistence check with the free-space case, the half-space case, and the multilayered case with symmetry. The free-space spectral Green's function is given by

$$\hat{G} = \frac{1}{4\pi u_0} \exp(-\sqrt{m_0} u_0 |z - z'|), \tag{44}$$

where $m_0 = 1$ and

$$u_0^2 = k_\rho^2 - k_0^2. \tag{45}$$

Meanwhile the half-space Green's function with zero boundary conditions on the half plane $z = 0$ is given by an image formula [21] as

$$\hat{G}_{half} = \frac{1}{4\pi u_0} \exp(-\sqrt{m_0} u_0 |z - z'|) - \frac{1}{4\pi u_0} \exp(-\sqrt{m_0} u_0 |z + z'|). \tag{46}$$

We apply formulas (42) and (43) with 5 fictitious layers (with layer locations $d_0 = 0,\ d_1 = -2,\ d_2 = -4, d_3 = -6,\ d_4 = -8$, and $k_i = m_i = 1$ for all layers) and $z = -3.0$ and $z' = -5.0$, and the result is compared with the exact free-space Green's function calculated using Eq. (44) along the positive real k_ρ axis in Fig. 3(a). In Fig. 3(b), for the fixed points $z = 5.0$ and $z' = 3.0$,

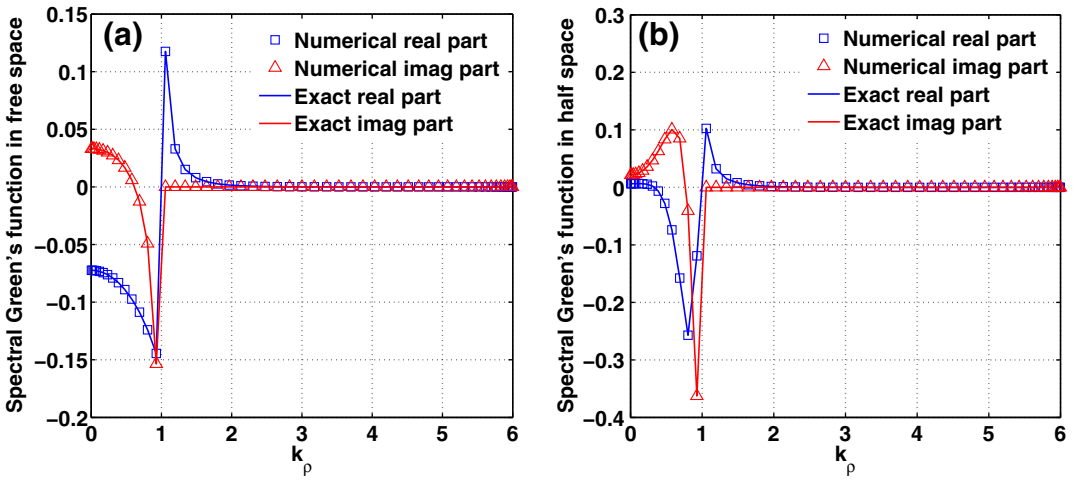

Fig. 3. (a) Free-space and (b) half-space spectral Green's functions calculated with the numerical method (marker) and the exact solution (solid line).

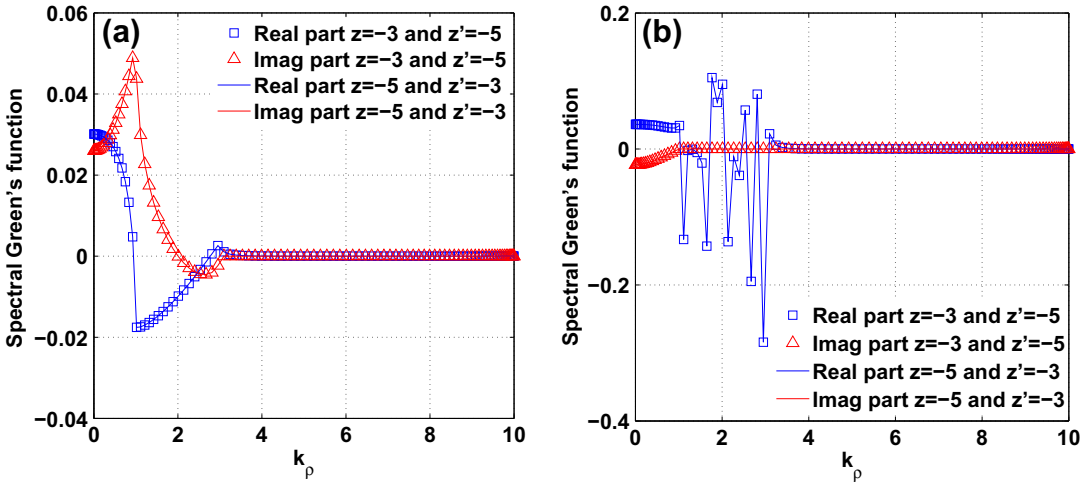

Fig. 4. Spectral Green's function for the multilayered structure with (a) $k_0 = 1,\ k_1 = 1,\ k_2 = 1,\ k_3 = 3,\ k_4 = 3,\ k_5 = 3$ and (b) $k_0 = 1,\ k_1 = 3,\ k_2 = 3,\ k_3 = 3,\ k_4 = 3,\ k_5 = 1$ for $z = -3$ and $z' = -5$ pair (marker) and $z = -5$ and $z' = -3$ pair (solid line).

the half-space spectral Green's function consisting of 5 fictitious layers (with layer locations $d_0 = 8,\ d_1 = 6,\ d_2 = 4,\ d_3 = 2,\ d_4 = 0$, and $k_i = m_i = 1$ for all layers) and with perfect electric conductor ($z < 0$) is calculated with the terminal condition given by Eq. (41). In both free- and half-spaces, numerical solutions agree well with the exact solutions. For a general multilayer medium, we can verify the formulas (42) and (43) by checking the symmetries of the Green's function for a symmetric profile of layer parameters. Fig. 4(a) and (b) show the spectral Green's functions for $k_0 = 1,\ k_1 = 1,\ k_2 = 1,\ k_3 = 3,\ k_4 = 3,\ k_5 = 3$ and $k_0 = 1,\ k_1 = 3,\ k_2 = 3,\ k_3 = 3,\ k_4 = 3,\ k_5 = 1$, respectively. The blue[1] and red solid lines are real and imaginary parts of $\hat{G}$ calculated with $z = -3$ and $z' = -5$, and the blue squares and red triangles are real and imaginary parts of $\hat{G}$ calculated with $z = -5$ and $z' = -3$. The two calculated spectral Green's functions overlap each other consistent with the symmetry of the structure.

3. Green's function in real space

The Green's function in real space can be obtained from the Green's function in the spectral domain with the 0th order Hankel transform, namely,

[1] For interpretation of colour in Figs. 6, 9, 10, 13–15 the reader is referred to the web version of this article.

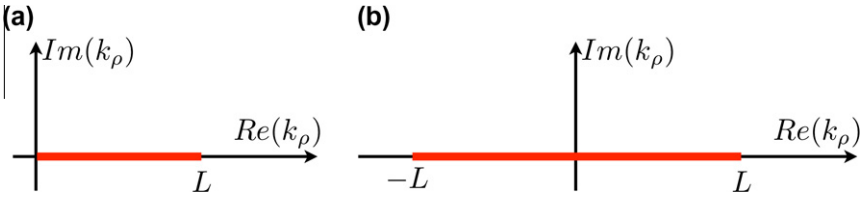

Fig. 5. (a) Integral contour for the Hankel transform for the tree-code version solver and (b) the wFMM version solver (mirror image of the contour in (a)).

$$G(\rho;z,z') = \int_0^\infty \widehat{G}(k_\rho;z,z')J_0(k_\rho\rho)k_\rho dk_\rho \approx \int_0^L \widehat{G}(k_\rho;z,z')J_0(k_\rho\rho)k_\rho dk_\rho \approx \sum_{s=0}^{N_q} w_s \widehat{G}(k_\rho^s;z,z')J_0(k_\rho^s\rho)k_\rho^s, \tag{47}$$

where the integral is truncated at the length L (see Fig. 5(a)), and k_ρ^s and w_s are quadrature points and weights, respectively. This numerical integration Eq. (47) has two difficulties. The first difficulty comes from the surface poles in the real axis of the complex k_ρ plane [25]. In order to remove the pole effects, a discrete wavelet transform (DWT) [5,6] is used to identify the pole locations and then adaptive generalized Gaussian quadratures are used. The second difficulty is the size of the contour length L due to the slow decay of the spectral Green's function when $z \sim z'$ or $z = z'$. For this matter, the window function is used to enhance the decay of the spectral Green's function or to shorten the truncation of the integral domain L. In the following subsections, the adaptive generalized Gaussian quadratures and window function techniques are presented.

3.1. Adaptive quadrature points with wavelets

The spectral Green's function has an oscillatory and $x^{-1/2}$ singular behavior (near the surface poles) along the real axis of the complex k_ρ space, therefore an adaptive and specially designed quadrature formula will be used to reduce the number of quadrature points N_q in Eq. (47); this plays an important role in the overall cost of the fast algorithm. At the same time, an accurate quadrature rule for $x^{-1/2}$ is necessary. First, surface pole locations are found using DWT (see Refs. [5,6] for details) as can be seen in Fig. 6, which shows the real part of the integrand of the Hankel transform (right axis) and wavelet collocation points (left axis) calculated with layer locations $d_0 = 0,\ d_1 = -2,\ d_2 = -4,\ d_3 = -6,\ d_4 = -8$ and $k_0 = 5,\ k_1 = 2,\ k_2 = 4,\ k_3 = 3,\ k_4 = 4,\ k_5 = 5$, and $z = -3$ and $z' = -5$ as a function of k_ρ from 0 to 5. The locations of singular behaviors are well detected with wavelet collocation points, and these can be used to construct an adaptive quadrature rule for the Hankel transform with generalized Gaussian quadrature for $x^{-1/2}$ by Ma et al. [23]. In detail, denote the singular

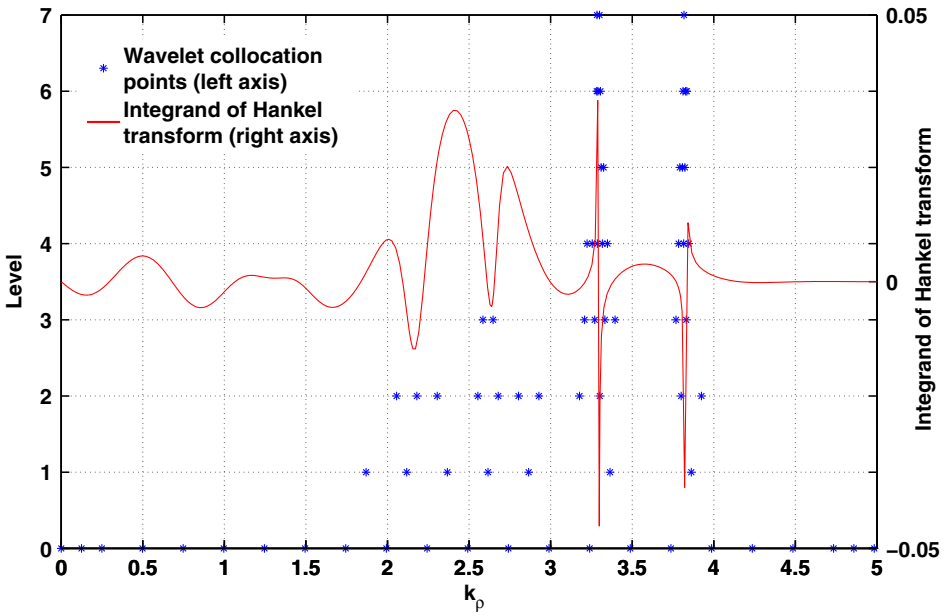

Fig. 6. Singular behavior detection with wavelets. The red solid line (right axis) represents the integrand of the Hankel transform and blue asterisks (left axis) are wavelet collocation points at each level with layer locations $d_0 = 0,\ d_1 = -2,\ d_2 = -4,\ d_3 = -6,\ d_4 = -8$ and $k_0 = 5,\ k_1 = 2,\ k_2 = 4,\ k_3 = 3,\ k_4 = 4,\ k_5 = 5$, and $z = -3$ and $z' = -5$.

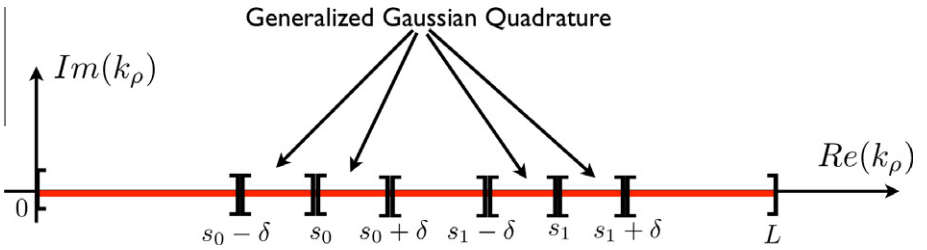

Fig. 7. Adaptive generalized Gaussian quadrature with two surface poles s_0 and s_1.

points by s_i, then the generalized Gaussian quadratures (*3–5 quadrature points are used*) can be used in the intervals $[s_i-\delta, s_i]$ and $[s_i, s_i+\delta]$ for a given positive δ, and normal Gaussian quadrature is used in all other intervals (see Fig. 7).

Fig. 8 is drawn to show how the performance of the adaptive quadrature combined with the generalized Gaussian quadratures compares with the uniform quadrature, which consists of equally spaced intervals with several Gaussian quadrature points in them. First, in Fig. 8(a), the real part of the free-space Green's functions are calculated with 200 uniform (triangle) and 20 (circle), 35 (square), and 65 (cross) adaptive quadrature points. The solution calculated with the uniform quadratures visibly differs from the exact solution (solid line) calculated with Eq. (52). Fig. 8(b) displays the relative errors between the exact and numerical solution calculated with 200 uniform (triangle) and 20 (circle), 35 (square), and 65 (cross) adaptive quadrature points. *Only one tenth of the quadrature points are necessary to outperform the uniform quadratures*. Fig. 8(c) shows the multilayer Green's functions calculated with 109 (circle) and 205 (square) adaptive and 1000 uniform (triangle) quadrature points compared with the reference solution (solid line), which is calculated with 1309 adaptive quadrature points (see the figure caption for the computation parameters). Again, 109 adaptive quadrature points performs better than

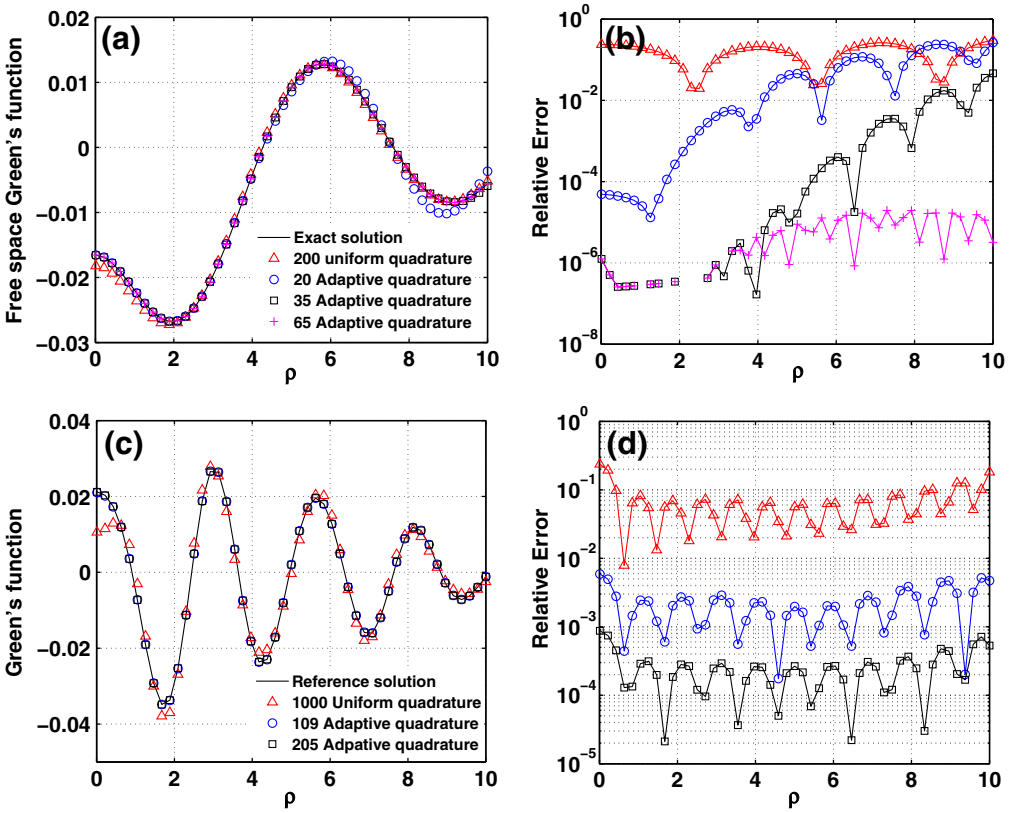

Fig. 8. (a) Real part of the free-space Green's function ($k_i = m_i = 1.0$ in all layers) calculated with uniform and adaptive quadrature points, and the exact solution (see the legends in the figure) and (b) relative error between the exact solution and the solution calculated with uniform and adaptive quadratures (see the legends in (a)). (c) Real part of the multilayer Green's function ($k_0 = 5,\ k_1 = 2,\ k_2 = 4,\ k_3 = 3,\ k_4 = 4,\ k_5 = 5$) calculated with uniform and adaptive quadrature rules (see the legends in figure), and (d) relative error between the reference solution and the numerical solution with various quadratures (see the legends in (c)). For all calculations, $z_i = 0, -2, -4, -6, -8$ and $z = -3$ and $z' = -5$ are used.

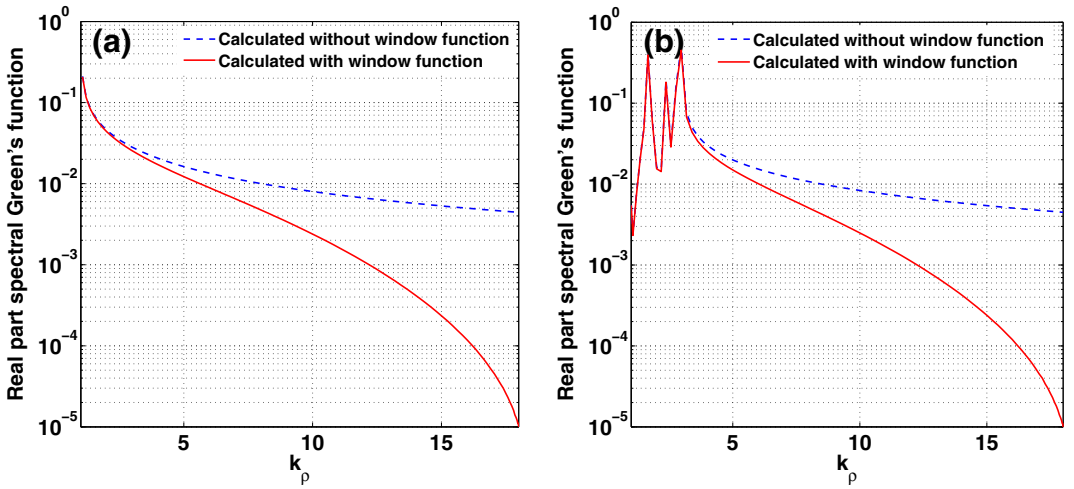

Fig. 9. Real part of the spectral Green's function calculated without (blue dashed line) and with (red solid line) window functions (window support $a = 0.6$ and order $m = 6$) for (a) free-space with 5 fictitious layers with $k_i = m_i = 1$ and (b) multilayered structure with $k_0 = 1,\ k_1 = 3,\ k_2 = 3,\ k_3 = 3,\ k_4 = 3$, and $k_5 = 1$ when $z = z' = -4$.

1,000 uniform quadrature points. In order to see the difference more quantitatively, relative errors between the reference solution and the numerical solution calculated with adaptive and uniform quadrature points are displayed in Fig. 8(d).

In conclusion, the adaptive quadrature combined with generalized Gaussian quadrature can achieve almost 10 times better accuracy with 10% quadrature points compared with the uniform one. This reduction of quadrature points will play a key role in optimizing the fast solver in a later section since it determines the number of tree-code or wFMM calls.

3.2. Hankel transform with window functions

When z is very close or equal to z', the spectral Green's function decays slowly (for example, the free- and half-space spectral Green's functions in Eqs. (44) and (46) decay as $(k_\rho^2 - k_0^2)^{-1/2}$ along the real k_ρ axis). As a consequence, the truncation of the integral domain L has to be large, and the number of quadrature points will be increased as a result. In order to overcome this problem, a window function method is proposed in Ref. [8]. According to the Algorithm 1 in this reference, the Hankel transform (Eq. (47)) is modified and approximated for $\rho > a$ by

$$G(\rho; z, z') = \frac{1}{M_0} \int_0^\infty \widehat{G}(k_\rho; z, z') J_0(k_\rho \rho) \hat{\psi}(k_\rho) k_\rho dk_\rho + O(a^2), \tag{48}$$

where the window function $\psi(k_\rho)$ in real space and $\hat{\psi}(k_\rho)$ in the spectral domain are defined by

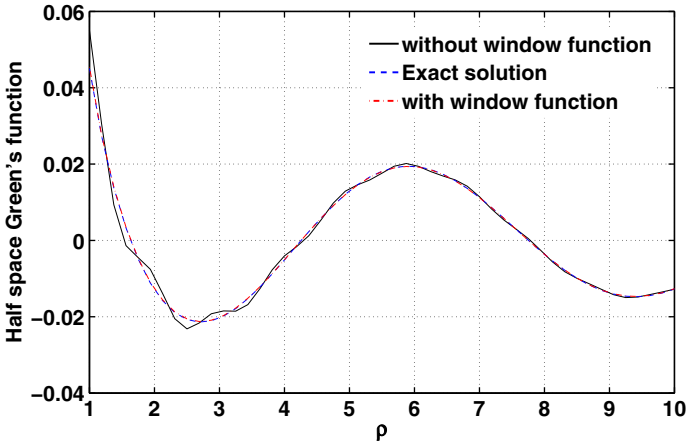

Fig. 10. Half-space Green's function calculated without (black solid line) and with (dash-dot red line) window functions and exact solution (dashed blue line) when $z = z' = 4$.

$$\psi_a(\rho) = \begin{cases} (1-(\frac{\rho}{a})^2)^m, & \text{if } \rho \leqslant a \\ 0, & \text{otherwise} \end{cases}, \tag{49}$$

$$\hat{\psi}_a(k_\rho) = \int_0^\infty \psi_a(\rho) J_0(k_\rho \rho) k_\rho dk_\rho \tag{50}$$

and

$$M_0 = \frac{1}{2\pi} \int_{\rho \leqslant a} \psi_a(\rho) d\rho = \frac{a^2}{2(m+1)}. \tag{51}$$

The closed forms and their approximations of window functions in the spectral domain (Eq. (50)) are given in Ref. [33], and included here for completeness in Appendix A.

The free-space and multilayer spectral Green's function calculated with (solid line) and without (dashed line) window functions when $z = z'$ are plotted in Fig. 9(a) and (b), respectively. Both figures show the slow decay of the spectral Green's function and the enhancement of decay from the window functions. Fig. 10 depicts the half-space Green's function when $z = z' = 4$ calculated with (dash-dotted line) and without (solid line) window functions compared with the exact solution (dashed line). $L = 20$ is used for all of the following calculations.

Now, Green's functions in layered structures will be calculated with the techniques presented in previous subsections. For fixed points $z = -3$ and $z' = -5$, the numerical solution from Eq. (47) with 5 fictitious layers (with layer locations $d_0 = 0,\ d_1 = -2,\ d_2 = -4, d_3 = -6,\ d_4 = -8$ and $k_i = m_i = 1,\ i = 0, 1, \ldots, 5$) and the exact free-space Green's function,

$$G(\rho; z, z') = \frac{e^{-jk\sqrt{m(\rho^2+(z-z')^2)}}}{4\pi\sqrt{\rho^2+(z-z')^2}}, \tag{52}$$

where

$$\rho = \sqrt{(x-x')^2+(y-y')^2},$$

are plotted as a function of ρ in Fig. 11(a). In addition, for the fixed points $z = 5.0$ and $z' = 3.0$, the half-space Green's function with 5 fictitious layers ($d_0 = 8,\ d_1 = 6,\ d_2 = 4,\ d_3 = 2, d_4 = 0$ and $k_i = m_i = 1,\ i = 0, 1, \ldots, 4$) with perfect conductor ($z < 0$) is calculated in Fig. 11(b). The numerical solution agrees very well with the exact half-space Green's function obtained with the image method, namely,

$$G_{half} = \frac{e^{-jk\sqrt{m(\rho^2+(z-z')^2)}}}{4\pi\sqrt{\rho^2+(z-z')^2}} - \frac{e^{-jk\sqrt{m(\rho^2+(z+z')^2)}}}{4\pi\sqrt{\rho^2+(z+z')^2}}. \tag{53}$$

Finally, in Fig. 11(c) and (d), two different multilayered structures are considered with $k_0 = 1,\ k_1 = 1,\ k_2 = 1,\ k_3 = 3, k_4 = 3$, and $k_5 = 3$ and $k_0 = 1,\ k_1 = 3,\ k_2 = 3,\ k_3 = 3, k_4 = 3$, and $k_5 = 1$, respectively, and with m_i assumed to be 1 in all layers for both figures. The symmetry is tested by switching z and z' in both figures. In both cases, the two solutions obtained with $z = -3$ and $z' = -5$ and $z = -5$ and $z' = -3$ are found to be the same because of the symmetry properties of the structure.

4. Fast algorithms for computing the Helmholtz integral operator in layered media

With the layered media Green's function developed in the previous section, parallel fast algorithms for the Helmholtz integral operator in layered media are proposed in this section.

The computation of the integral in Eq. (47) is accelerated with the 2-D wFMM for the complex Helmholtz equation [10,11] as suggested in [7]. In order to use wFMM, the integral domain in Eq. (47) is extended with its mirror image using symmetry as in Fig. 5(b), and the Bessel function is replaced by the Hankel function as follows:

$$G(\rho; z, z') = \frac{1}{2M_0} \int_{-\infty}^{\infty} \widehat{G}(k_\rho; z, z') H_0^{(1)}(k_\rho \rho) \hat{\psi}_a(k_\rho) k_\rho dk_\rho. \tag{54}$$

Next, the integral in Eq. (54) is discretized with adaptive quadrature points (k_ρ^s) and weights (w_s) proposed in Section 3.1 as

$$G(\rho; z, z') = \frac{1}{2M_0} \sum_{s=1}^{2N_q} w_s \hat{G}(k_\rho^s; z, z') H_0^{(1)}(k_\rho^s \rho) \hat{\psi}_a(k_\rho^s) k_\rho^s = \frac{1}{2M_0} \sum_{s=1}^{2N_q} \Gamma_s \widehat{G}(z, z', k_\rho^s) H_0^{(1)}(k_\rho^s \rho), \tag{55}$$

where

$$\Gamma_s = w_s \hat{\psi}_a(k_\rho^s) k_\rho^s \tag{56}$$

and N_q is the number of quadrature points in the positive real axis. Assume that there are $N_z = O(1)$ layers and $|\Delta| = O(N_x N_y)$ points in each layer. Then, for each point $(x_i^k, y_j^k) \in \Delta,\ 1 \leqslant k \leqslant N_z$, the Helmholtz integral operator in layered media $\phi(x_i^k, y_j^k, z_k)$ can be calculated as follows using Eq. (55):

$$\phi(x_i^k, y_j^k, z_k) = \sum_{m,n,l} G(x_i^k, y_j^k, z_k; x_m^{l'}, y_n^{l'}, z_l') J(x_m^{l'}, y_n^{l'}, z_l') \tag{57}$$

$$= \frac{1}{2M_0} \sum_{m,n,l} \sum_{s=1}^{2N_q} \Gamma_s \hat{G}(z_k, z_l', k_\rho^s) H_0^{(1)}(k_\rho^s \rho) J(x_m^{l'}, y_n^{l'}, z_l')$$

$$= \frac{1}{2M_0} \sum_{s=1}^{2N_q} \Gamma_s \sum_{l} \hat{G}(z_k, z_l', k_\rho^s) \sum_{m,n} H_0^{(1)}(k_\rho^s \rho) J(x_m^{l'}, y_n^{l'}, z_l')$$

$$= \frac{1}{2M_0} \sum_{s=1}^{2N_q} \Gamma_s \sum_{l} \hat{G}(z_k, z_l', k_\rho^s) \psi_s(x_i^k, y_j^k, z_l'), \tag{58}$$

where

$$\rho_{i,j;m,n} = \sqrt{(x_i^k - x_m^{l'})^2 + (y_j^k - y_n^{l'})^2} \tag{59}$$

and

$$\psi_s(x_i^k, y_j^k, z_l') = \sum_{m,n} H_0^{(1)}(k_\rho^s \rho_{i,j;m,n}) J(x_m^{l'}, y_n^{l'}, z_l'). \tag{60}$$

Now, for each fixed pair z_k and z_l', ψ_s is the cylindrical wave integral operator, and it can be evaluated for all positive k_ρ^s with wFMM in a fast manner, and can be reused for negative k_ρ^s (i.e. the mirror-imaged integral contour) due to the symmetry of the Hankel function.

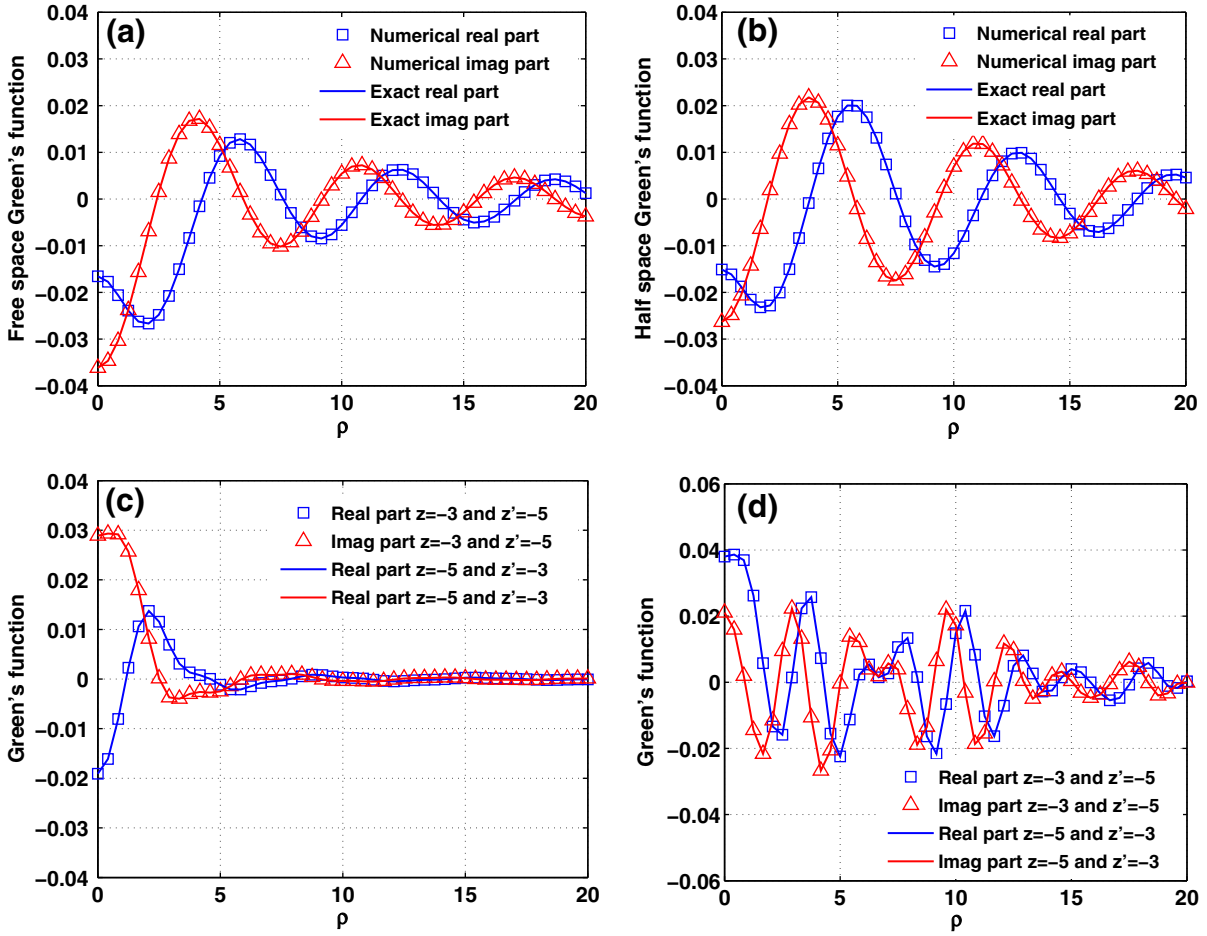

Fig. 11. The Green's function for (a) free-space ($k_i = m_i = 1$ with $z = -3$ and $z' = -5$) calculated with numerical method (marker) and the exact solution (solid line), (b) half-space ($k_i = m_i = 1$ with $z = 5$ and $z' = 3$) calculated with the numerical method (marker) and the exact solution (solid line), (c) the multilayered structure with $k_0 = 1,\ k_1 = 1,\ k_2 = 1,\ k_3 = 3,\ k_4 = 3$, and $k_5 = 3$ with the pair $z = -3$ and $z' = -5$ (marker) and the pair $z = -5$ and $z' = -3$ (solid line), and (d) the multilayered structure with $k_0 = 1,\ k_1 = 3,\ k_2 = 3,\ k_3 = 3,\ k_4 = 3$, and $k_5 = 1$ with the pair $z = -3$ and $z' = -5$ (marker) and the pair $z = -5$ and $z' = -3$ (solid line).

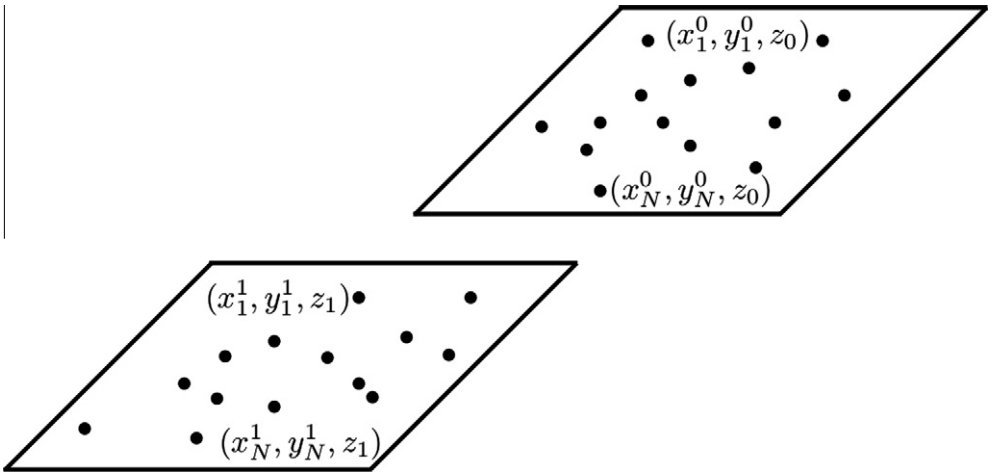

Fig. 12. Two layers of randomly distributed unknown points.

In the derivation of the fast algorithm, the integral domain is extended to the negative axis in order to utilize wFMM. However, a 2-D local expansion tree-code for the 0th order Bessel function can be easily developed and implemented based on our wFMM code (see Appendix B) with the same computational complexity and with a smaller prefactor. Moreover, two big advantages of the tree-code over the wFMM are that it does not require time-consuming multipole-to-local conversion operations and wideband treatment in wFMM. As a consequence, the tree-code is expected to be more efficient and faster than wFMM. Now we derive the tree-code version fast solver directly from Eq. (47) for the positive integral contour only. First, the Helmholtz integral operator in layered media (Eq. (58)) can be rewritten as

$$\phi(x_i^k, y_j^k, z_k) = \frac{1}{M_0}\sum_{s=1}^{N_q} \Gamma_s \sum_l \hat{G}(z_k, z_l', k_\rho^s)\psi_s(x_i^k, y_j^k, z_l'), \tag{61}$$

where

$$\psi_s(x_i^k, y_j^k, z_l') = \sum_{m,n} J_0(k_\rho^s \rho_{i,j;m,n}) J(x_m^{l'}, y_n^{l'}, z_l'). \tag{62}$$

The ψ_s can be calculated with the 2-D tree-code for the 0th order Bessel function only for positive quadrature points.

The operation counts for both solvers are $O(N_q N_z^2 N_x N_y \log N_x N_y)$, where N_x, N_y, and N_z are the number of unknown points in the x-, y-, and z-axis, respectively. N_z is much smaller than N_x and N_y for thin layers which is the case for many applications. Therefore, the choice of N_q plays an important role in the overall cost of the fast algorithm.

Fig. 13 shows the CPU time of the tree-code version (Eq. (61)) and wFMM version (Eq. (58)) fast algorithms compared with direct calculation (Eq. (57)) for the half-space. Fig. 13(a) is redrawn as (b) (with x-axis truncated at 100,000) to show the break-even point. Five fictitious layers $d_0 = 8$, $d_1 = 6$, $d_2 = 4$, $d_3 = 2$, $d_4 = 0$ with $k_i = m_i = 1$, $i = 0, 1, \ldots, 5$, and the

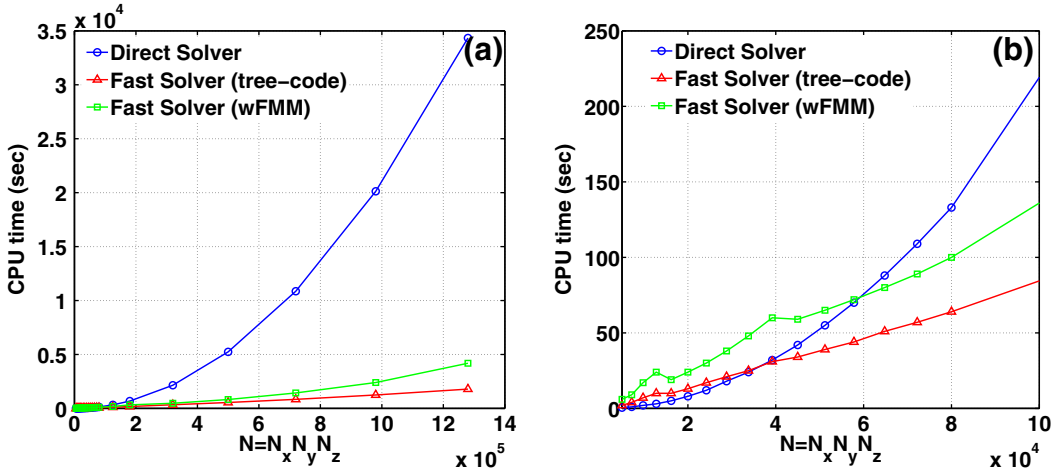

Fig. 13. (a) CPU time (sec) for the direct solver (blue circle), FMM version fast solver (green square), and tree-code version fast solver (red triangle) for the half-space. (b) N is truncated at 100,000 to show the break-even point.

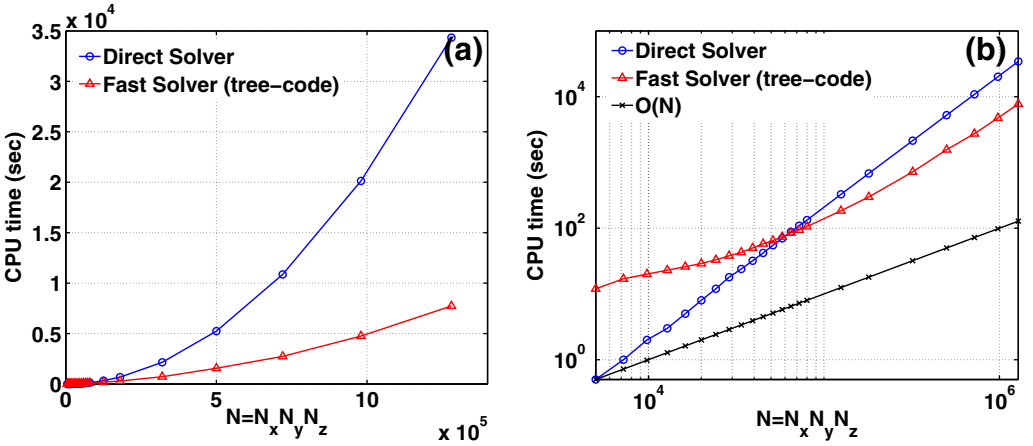

Fig. 14. (a) CPU time of the direct (blue circle) and tree-code version fast solver (red triangle) for the multilayer Green's function with layer locations $d_0 = 0,\ d_1 = -2,\ d_2 = -4,\ d_3 = -6,\ d_4 = -8$ and $k_0 = 5,\ k_1 = 2,\ k_2 = 4,\ k_3 = 3,\ k_4 = 4,\ k_5 = 5$ and an unknown layer located at $z = -3$ and $z = -5$. (b) CPU time in the log–log scale to show the computational complexity and the break-even point between direct and fast solver for the multilayer Green's function. The $O(N)$ (black cross) plot is added only for a comparison purpose.

perfect conductor ($z < 0$) are used to calculate the Green's function at two layers ($N_z = 2$) of random unknown points $N_x \times N_y$ in boxes $[2.5, 3.5] \times [-0.5, 0.5]$ located at $z = 5$ and $[-0.5, 0.5] \times [-0.5, 0.5]$ located at $z = 3$ (see Fig. 12 for an illustration).

The number of unknown points $N_x \times N_y \times N_z$ are varied from $50 \times 50 \times 2$ to $800 \times 800 \times 2$, and the outer sum on k_ρ^s (15 quadrature points for 1% relative error) is parallelized with OpenMP for multicore shared memory systems [26]. Computations are conducted with a machine consisting of two quad-core Intel Xeon 3.00 GHz processors, 32 GB memory, and a gcc version 4.5.1 running on Fedora release 11. The CPU time increases quadratically for the direct calculation and $O(N_q N_x N_y \log N_x N_y)$ with $N_z = 2$ for the fast solvers as predicted. The break-even point between the direct and wFMM version fast solver is around 60,000 points and the tree-code version is 35,000 (see Fig. 13(b)). The tree-code version solver is found to be faster than the wFMM version fast algorithm as expected. Note that any numerical tools can be used to accelerate the calculation of ψ_s depending on user's preference.

In addition to the half-space, a multilayer (with layer locations $d_0 = 0,\ d_1 = -2,\ d_2 = -4,\ d_3 = -6,\ d_4 = -8$ and $k_0 = 5,\ k_1 = 2,\ k_2 = 4,\ k_3 = 3,\ k_4 = 4,\ k_5 = 5$ and $m_i = 1,\ i = 0, 1, \ldots, 5$), with two layers ($N_z = 2$) of random unknown points $N_x \times N_y$ in boxes $[2.5, 3.5] \times [-0.5, 0.5]$ located at $z = -3$ and $[-0.5, 0.5] \times [-0.5, 0.5]$ located at $z = -5$, is considered in Fig. 14. The number of unknown points in the thin layer $N = N_x \times N_y \times N_z$ is varied from $50 \times 50 \times 2$ to $800 \times 800 \times 2$. The tree-code version fast solver with $N_q = 40$ (red triangle) quadrature points, which yields 7% relative error, is compared with the direct calculation (blue circle) in terms of the CPU time. The break-even point was found to be at approximately $N = 62{,}000$, and it will increase as the number of quadrature points increases (or if a higher accuracy is required) because

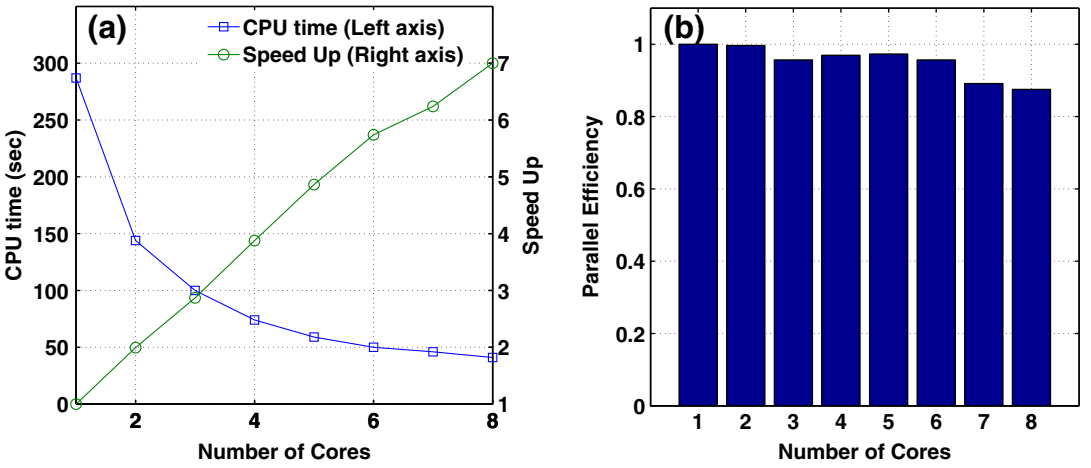

Fig. 15. (a) CPU time in seconds (blue square, left axis) and calculation speed increase compared to single-core CPU time (green circle, right axis) as a function of the number of cores and (b) the parallel efficiency.

Table A.1
Coefficients for the window functions from 1st to 7th order.

m	1	2	3	4	5	6	7
$H_{m0}\cdot 10^2$	25	16.6667	12.5	10	8.33333	7.1428571	6.25
$H_{m1}\cdot 10^3$	20.83333	10.41667	6.25	4.166666	2.9761905	2.2321429	1.7361111
$H_{m2}\cdot 10^5$	65.1041666	26.04166	11.574074	7.440476	4.650297	3.100198	2.170138
$H_{m3}\cdot 10^7$	108.5069444	36.16898	15.50099	7.750496	4.305831	2.583498	1.644044
$H_{m4}\cdot 10^{10}$	1130.28067	322.9373	121.1015	53.82288	26.91144	14.67897	8.562732
$H_{m5}\cdot 10^{12}$	807.343336	201.8358	67.27861	26.91144	12.23247	6.116237	3.293358
$H_{m6}\cdot 10^{15}$	4204.9132	934.4251	280.3275	101.9372	42.47387	19.60332	9.801662

the tree-code must be called at each additional quadrature point. Fig. 14(a) is redrawn with the log–log scale in Fig. 14(b) to show the computational complexity. The $O(N)$ complexity line (cross) is added only for a comparison purpose.

Finally, in Fig. 15, the parallel efficiency for the half-space is plotted with $N = 225{,}000$ as the number of CPU cores increases from 1 to 8. When 8 cores are used, it is 7 times faster than the single core CPU time.

5. Conclusions

Parallel fast algorithms for the Helmholtz integral operator in 3-D layered media based on the tree-code for the Bessel function and the wFMM for the Hankel function are implemented, and their efficiencies are investigated. In computing the Hankel transform for the layered media Green's functions, adaptive quadrature rules with a discrete wavelet transform for pole singularity identifications are used to remove surface pole effects, and the window function is utilized to enhance the decay of the spectral Green's function for fast convergence. The proposed algorithms can be implemented with a high degree of parallelism with respect to the quadrature point N_q, namely, the computation for each of the quadrature points can be done independently using separate processors. More rigorous optimization and massive parallelization are under study and will be reported elsewhere. Finally, the fast algorithm will be applied to many possible applications in electromagnetics and quantum mechanics such as quantum dots [34] and surface plasmons in thin structured films [17].

Acknowledgments

This work is supported in part by the US army office of research (Grant No. W911NF-11-1-0364), NSF grant DMS-1005441 and the US Department of Energy (Grant No. DEFG0205ER25678). The authors would like to acknowledge Prof. Jingfang Huang at UNC Chapel Hill, Prof. Robert Krasny at U. of Michigan, Dr. Hengliang Zhu at Fudan University, and Mr. Mark Hamrick at UNC Charlotte for valuable comments and help regarding FMM, tree-code, DWT, and computing support, respectively.

Appendix A. Closed form of the window functions

Here the closed forms and their approximations of the window functions are provided up to the 7th order.

- The case $k_\rho a < 1$:
  Using the taylor expansion of the Bessel function [1],

$$J_n(z) = \sum_{k=0}^{\infty} \frac{(-1)^k}{k!} \frac{1}{(n+k)!} \left(\frac{z}{2}\right)^{2k+n}, \tag{A.1}$$

the window function in the spectral domain can be written as

$$\hat{\psi}_a(k_\rho) = \int_0^a \left(1 - \left(\frac{\rho}{a}\right)^2\right)^m J_0(k_\rho \rho)\rho d\rho \tag{A.2}$$

$$= a^2 \sum_{i=0}^{m} \sum_{j=0}^{\infty} h_{i,j} y^{2j} \tag{A.3}$$

$$\approx a^2 (H_{m0} - y^2(H_{m1} - y^2(H_{m2} - y^2(H_{m3} - y^2(H_{m4} - y^2(H_{m5} - y^2 H_{m6})))))), \tag{A.4}$$

where $y = k_\rho a$ and the coefficients $H_{mj},\ j = 0, 1, \ldots, 6$ are given in Table A.1.

- The case $k_\rho a \geqslant 1$:
  Using the Lommel function and Bessel functions, the window function in the spectral domain can be expressed as follows:

$$\hat{\psi}_a(k_\rho) = g_m, \tag{A.5}$$

where

$$g_1 = \frac{a^2}{y^2}\left[-2J_0(y) + \frac{4}{y}J_1(y)\right], \tag{A.6}$$

$$g_2 = \frac{a^2}{y^2}\frac{8}{y}\left[-\frac{4}{y}J_0(y) + \left(\frac{8}{y^2} - 1\right)J_1(y)\right], \tag{A.7}$$

$$g_3 = \frac{a^2}{y^2}\frac{48}{y^2}\left[\left(1 - \frac{24}{y^2}\right)J_0(y) - \frac{8}{y}\left(1 - \frac{6}{y^2}\right)J_1(y)\right], \tag{A.8}$$

$$g_4 = \frac{a^2}{y^2}\frac{182}{y^3}\left[\frac{24}{y}\left(1 - \frac{16}{y^2}\right)J_0(y) + 2\left(1 - \frac{24}{y^2}\left(3 - \frac{16}{y^2}\right)\right)J_1(y)\right], \tag{A.9}$$

$$g_5 = \frac{a^2}{y^2}\frac{1920}{y^4}\left[\left(-2 + \frac{96}{y^2}\left(3 - \frac{40}{y^2}\right)\right)J_0(y) + \frac{1}{y}\left(36 - \frac{1536}{y^2}\left(1 - \frac{5}{y^2}\right)\right)J_1(y)\right], \tag{A.10}$$

$$g_6 = \frac{a^2}{y^2}\frac{46080}{y^5}\left[\frac{24}{y}\left(-1 + \frac{80}{y^2}\left(1 - \frac{12}{y^2}\right)\right)J_0(y) + \left(-1 + \frac{96}{y^2}\left(3 - \frac{20}{y^2}\left(5 - \frac{24}{y^2}\right)\right)\right)J_1(y)\right], \tag{A.11}$$

$$g_7 = \frac{a^2}{y^2}\frac{645120}{y^6}\left[\left(1 - \frac{480}{y^2}\left(1 - \frac{4}{y^2}\left(15 - \frac{168}{y^2}\right)\right)\right)J_0(y) + \frac{32}{y}\left(-1 + \frac{5}{y^2}\left(30 - \frac{144}{y^2}\left(6 - \frac{28}{y^2}\right)\right)\right)J_1(y)\right]. \tag{A.12}$$

Appendix B. Local expansion tree-code for Bessel function in 2-D

The downward pass of the 2-D FMM algorithm [18] is used to implement local expansion tree-code. In this tree-code, far-field signature of the J-expansion (local expansion) is directly constructed from the interaction list rather than converted from the multipole expansion in FMM. Then, it is shifted to its children boxes with a diagonalized operator and added with the far-field signature constructed from the interaction list of the children box. This procedure continues until the bottom of the tree data structure is reached. At the childless boxes, the far-field signature is evaluated at each particle location and added with direct interaction between particles in the close-neighbor boxes and itself. All the necessary formulas for the implementation of tree-code are given below. All the analysis and formula follow exactly from the [27].

- J-expansion:
  Assume N particles q_k are located at $r_k = (x_k, y_k)$, $k = 1, 2, \ldots, N$, outside of a disc D_1 centered at c_1. Then for any point r inside of D_1, the radiation field due to N particles can be written as

$$\psi_{c_1}(r) = \sum_{k=1}^{N} J_0(\omega|r - r_k|)q_k = \sum_{m=-\infty}^{+\infty} \alpha_m J_m(\omega\rho_1)e^{-im\theta}, \tag{B.1}$$

where

$$\alpha_m = \sum_{k=1}^{N} q_k J_0(k|r_k|)e^{im\theta_k}, \tag{B.2}$$

$\rho_1 = |r - c_1|$, and θ and θ_k are angles between $r - c_1$ and the x-axis and $r_k - c_1$ and the x-axis, respectively. This formula is a direct consequence of the addition theorem for Bessel functions [1].

- J-2-J operation:
  Assume

$$\psi_{c_1}(r) = \sum_{m=-\infty}^{+\infty} \alpha_m J_m(\omega\rho_1)e^{-im\theta_1} \tag{B.3}$$

is analytic for any $r \in D_1$ centered at c_1, where $\rho_1 = |r - c_1|$ and θ_1 is the angle between ρ_1 and the x-axis. Then, in a disc D_2 centered at c_2, the potential can be written as

$$\psi_{c_2}(r) = \sum_{m=-\infty}^{+\infty} \widetilde{\alpha_m} J_m(\omega\rho_2)e^{-im\theta_2}, \tag{B.4}$$

where

$$\widetilde{\alpha_m} = \sum_{j=-\infty}^{+\infty} e^{ij(\theta_{12} - \pi)}\alpha_{m-j}J_j(k\rho_{12}), \tag{B.5}$$

$\rho_2 = |r - c_2|$, $\rho_{12} = |r_2 - r_1|$, θ_2 and θ_{12} are the angles between ρ_2 and the x-axis and ρ_{12} and the x-axis, respectively. Again, this operation is a direct application of the addition theorem.

- Far-field signature G of the J-expansion:

$$G(\theta) = \sum_{m=-\infty}^{\infty} \alpha_m e^{-i(m\pi/2)} e^{im\theta}, \tag{B.6}$$

where $\{\alpha_m\}_{m=-\infty}^{+\infty}$ are the coefficients of the J-expansion.

- Diagonalized G-2-G operation:
  Let

$$\mu(w) = e^{-ik\rho_{12}\sin(w-\theta_{12}-\pi)}. \tag{B.7}$$

Then, the far field expansion G_{c_1} in D_1 centered at c_1 can be translated to the far field expansion G_{c_2} in D_2 centered at c_2 by

$$G_{c_2}(w_j) = \mu(w_j) G_{c_1}(w_j), \tag{B.8}$$

where

$$w_j = \frac{2\pi j}{N}, \quad j = 0, 1, 2, \ldots, N-1. \tag{B.9}$$

References

[1] M. Abramowitz, I.A. Stegun, Handbook of Mathematical Functions, Dover, New York, 1970.
[2] M.I. Aksun, A robust approach for the derivation of closed-form Green's functions, IEEE Trans. Microw. Theory Tech. 44 (1996) 651–658.
[3] E. Bleszynski, M. Bleszynski, T. Jaroszewicz, AIM: adaptive integral method for solving large scale electromagnetic scattering and radiation problems, Radio Sci. 31 (1996) 1225–1251.
[4] O.P. Bruno, L.A. Kunyansky, High order algorithm for the solution of surface scattering problems: basic implementation, test, and applications, J. Comput. Phys. 169 (2001) 80–110.
[5] W. Cai, J. Wang, Adapative multiresolution collocation methods for initial boundary value problems of nonlinear PDEs, SIAM J. Numer. Anal. 33 (1996) 937–970.
[6] W. Cai, W. Zhang, An adapative spline wavelet ADI (SW–ADI) method for two-dimensional reaction–diffusion equations, J. Comput. Phys. 139 (1998) 92–126.
[7] W. Cai, Algorithmic issues for electromagnetic scattering in layered media: Green's functions, current basis, and fast solver, Adv. Comput. Math. 16 (2002) 157–174.
[8] W. Cai, T. Yu, Fast calculation of dyadic Green's functions for electromagnetic scattering in a multilayered medium, J. Comput. Phys. 165 (2000) 1–21.
[9] H. Cheng, W. Crutchfield, Z. Gimbutas, L. Greengard, J.F. Ethridge, J. Huang, V. Rokhlin, N. Yarvin, J. Zhao, A wideband fast multipole method for the Helmholtz equation in three dimensions, J. Comput. Phys. 216 (2006) 300–325.
[10] M.H. Cho, W. Cai, A wideband fast multipole method for the two-dimensional complex Helmholtz equation, Comput. Phys. Commun. 181 (2010) 2086–2090.
[11] M.H. Cho, W. Cai, Revision of wFMM – a wideband fast multipole method for the two-dimensional complex Helmholtz equation, Comput. Phys. Commun. 183 (2012) 446–447.
[12] Y.L. Chow, J.J. Yang, D.G. Fang, G.E. Howard, A closed form spatial Green's function for the thick microstrip substrate, IEEE Trans. Microw. Theory Tech. 39 (1991) 588–592.
[13] T.J. Cui, W.C. Chew, Fast evaluation of Sommerfeld integrals for EM scattering and radiation by three dimensional buried objects, Research Report No. CCEM-34-97, University of Illinois, Urbana, IL, 1997.
[14] T.J. Cui, W.C. Chew, Efficient evaluation of Sommerfeld integrals for TM wave scattering by buried objects, J. Electromagn. Wave Appl. 12 (1998) 607–657.
[15] W. Crutchfield, Z. Gimbutas, L. Greengard, J. Huang, V. Rokhlin, N. Yarvin, J. Zhao, Remarks on the implementation o f wideband FMM for the Helmholtz equation in two dimensions, Contemp. Math. 408 (2006) 99–110.
[16] <http://fastmultipole.org/>.
[17] C.H. Gan, G. Gbur, T.D. Visser, Surface plasmons modulate the spatial coherence of light in Young's interference experiment, Phys. Rev. Lett. 98 (2007) 043908.
[18] L.F. Greengard, The Rapid Evaluation of Potential Fields in Particle Systems, MIT Press, Cambridge, 1988.
[19] R.F. Harrington, Field Computation by Moment Method, Macmillian, New York, 1968.
[20] B. Hu, W.C. Chew, Fast inhomogeneous plane wave algorithm for electromagnetic solutions in layered medium structures: two-dimensional case, Radio Sci. 35 (1) (2000) 31–43.
[21] J.D. Jackson, Classical Electrodynamics, third ed., Wiley, 1998.
[22] S. Kapur, V. Rokhlin, An algorithm for the fast Hankel transform, Technical Report 1045, Computer Science Department, Yale University, 1995.
[23] J. Ma, V. Rokhlin, S. Wandzura, Generalized Gaussian quadrature rules for systems of arbitrary functions, Research report, YALEU/DCS/RR-990, 1993.
[24] E. Michielssen, W.C. Chew, Fast steepest descent path algorithm for analyzing scattering from two-dimensional objects, Radio Sci. 31 (1996) 1215–1224.
[25] J.R. Mosig, Integral equation technique, in: T. Itoh (Ed.), Numerical Techniques for Microwave and Millimeter-Wave Passive Structure, Wiley, New York, 1989, pp. 133–213.
[26] OpenMP, <http://openmp.org/wp/>
[27] V. Rokhlin, Rapid solution of integral equations of scattering theory in two dimensions, J. Comput. Phys. 86 (1990) 414–439.
[28] V. Rokhlin, Diagonal forms of translation operators for the Helmholtz equation in three dimensions, Appl. Comput. Harmon. Anal. 1 (1993) 82–93.
[29] Y. Saad, Iterative Methods for Sparse Linear Systems, PWS Publishing Company, 1996.
[30] P.P. Silvester, R.L. Ferrari, Finite Elements for Electrical Engineer, Cambridge Univ. Press, Cambridge, 1996.
[31] H.A. Van der Vorst, BI-CGSTAB: a fast and smoothly converging variant of Bi-CG for the solution of nonsymmetric linear systems, SIAM J. Sci. Stat. Comput. 13 (1992) 631–644.
[32] K.S. Yee, Numerical solution of initial boundary value problems involving Maxwell equations in isotropic media, IEEE Trans. Anten. Prop. 14 (1966) 302–307.
[33] T. Yu, W. Cai, High-order window functions and fast algorithms for calculating dyadic electromagnetic Green's functions in multilayered media, Radio Sci. 36 (2001) 559–569.
[34] Y. Yu, An integral equation approach for tunneling property of quantum dot, Ph.D Dissertation, The University of North Carolina at Charlotte, 2005.